SFWA

Final Report

Deliverable 4.3
JTI-CS-2010-4-SFWA-01-013 277975
Active Flow Control techniques on Trailing Edge Shroud for Improved High Lift Configurations (ATTESI)

Prepared by: **Lead Contributors** **Peter Scholz (TU-BS)**
Marcus Casper (TU-BS)
Stefan Wallin (FOI)
Stephan Adden (IBK)

Document control data

Internal Report No.:	***D4.3***	In accordance with DoW 277975
Version/Date:	**V1.0**	The Report leader: Peter Scholz, TU-BS
Approval		
Authorization		

1 Table of Contents

2 Introduction

The control of flow separation using active flow control is a promising application for future transport systems. For high-lift airfoils active flow control might lead to a significant reduction of the system's complexity, e.g. by using airfoils without moving parts at the leading edge ("slatless" airfoils), where the loss of maximum lift that is associated with the missing leading edge device is regained by active control of flow separation. One possibility for such a slatless airfoil to recover maximum lift is the application of vortex generator jets (VGJs). VGJs are a spanwise row of small orifices that are fed with pressurized air such that they create a local jet. The jet has an oblique orientation and therefore, very similar to static vane vortex generators, generates a longitudinal vortex embedded within the boundary layer—such structure is known to be able to suppress stall [2]. The size of the orifice is typically a fraction of the local boundary layer thickness; the jet exit velocity is quite high (often near the speed of sound). Several orifices are used in a spanwise row such that the macroscopic effect on the airfoil flow is quasi-2D. VGJs can be operated in a wide range of modes, e.g. pulsed or zero net-mass flux, but also in a steady mode (continuous blowing), [4][5].

Also the Gurney-flap is known to be able to increase maximum lift. The fluid mechanical effect is basically that a small scale plate at the trailing edge of a wing—approximately perpendicular to the airfoil chord—enforces a number of counter-rotating vortices that shift the effective rear stagnation point of the airfoil further downstream. Thus a pressure difference at the airfoil surface can remain that increases lift. A very similar concept, but based on a fluidic device is the "jet flap", where the effect is the same as with a gurney flap, but instead of a mechanical device an air jet is used. The principal advantage w.r.t. a mechanical Gurney is that integration might be easier, which is known to be a problem for mechanical Gurney devices, since they need to be retractable for cruise-flight. Herein, a fluidic actuator mimicking a Gurney will be called the "fluidic Gurney" (FG).

However, application of active means, may that be VGJs or a FG, to control flow separation must be well designed, because not only the effectiveness, but also the efficiency (effect per effort, for high-lift

airfoils this means: $\Delta C_{l,max}/C_\mu$) plays an important role. In order to bring out an efficient effect, the designer needs to find a place for the application, where a certain effect on the local flow can be turned into a major advantage.

Improvements of low-speed performance might come from the use of smart trailing edge devices. E.g. the Airbus A350 as well as the Boeing 787 feature spoiler devices that can droop downwards combined with special flap mechanisms: The idea is to use an incomplex flap-track mechanism, which is sometimes called a dropped hinge (i.e. the hinge line is well underneath the airfoil chord line, enabling the fowler-type motion of the flap) that replaces the heavy steel-tracks and carriages of conventional flap kinematics. Such a dropped hinge results in a wide gap between the main element and the flap, when the flap is extensively lowered during landing. This gap is then decreased by a spoiler droop, which is neither much additional effort, nor weight, because actuators and hinges exist anyway for applying the spoiler motion. The primary advantage of such mechanism is weight savings and not improved aerodynamics. However, a spoiler droop could also result in increased maximum lift, because the camber of the airfoil increases and the camber line curvature is distributed more evenly, which is advantageous for the boundary layer development and separation, consequently. It is counteracted by the detrimental influence of the kink that appears at the hinge line of the spoiler, which limits the maximum possible spoiler droop, because the flow will separate prematurely at the kink, i.e. drooped spoiler configurations require a design tradeoff between the positive effect of better camberline distribution and larger flap angle and the detrimental effect of a kink at the suction side.

The existence of two contradictory principles is an advantageous frame for the application of active flow control methods: they can be used to prevent premature separation at the spoiler kink, enabling more extensive spoiler droop and larger flap angles and thus greater maximum lift.

The work presented herein consists of four elements: The core element is design computations making use of 2D RANS simulations in an optimization suite. These design studies also include the effect of the VGJs on the flow by the use of a statistical model, [13][14]. In order to acquire calibration data for the statistical model and to gain detailed insight into the effect of the VGJs, also 3D RANS computations fully resolving the VGJs and the longitudinal vortices were performed on a supercomputer cluster. A selection of configurations was tested in a low-speed wind tunnel for validation. Last but not least a concept (including a physical demonstrator) for a smart surface above the spoiler kink has been developed, which smoothens the kink without influencing the operationality, thus further reducing the effect of the kink on the flow.

All studies herein make use of the so-called DLR-F15 airfoil as baseline geometry [6]. The setting of the flap and a droop of the spoiler are considered, while flap and spoiler shape were held constant.

3 Numerical Design (WP 2)

3.1 RANS-Studies with resolved vortices (WP 2, T2.3)

As will be explained in detail in the following section, in the statistical VGJ model the longitudinal vortices are represents by their “vortex stresses”, i.e. additional stresses that are added as a source term to the Reynolds stress tensor. A spanwise row of a VGJ configuration, that means their size and orientation, as well as the spacing in between individual orifices, is averaged into a “pattern” of stresses. This process requires exact knowledge about the distribution of these stresses. Although attempts are ongoing to find a general formulation [15], the approach here was to use RANS-data, where the vortices are explicitly resolved.

The respective computations were performed using the DLR-TAU-code, [12], using the approach of Mahmood et al., [3][9]. The grid consisted of 13 Mio grid cells, 12 Mio of which were in the near field in multiple hexahedral cell blocks. The far field was discretized with approximately 1 Mio tetrahedral cells. The cells were highly clustered in the region of the VGJs and downstream, where significant gradients of the primary flow variables were expected. The mesh itself was three-dimensional in order to allow for the discrete VGJ orifice. However, the mesh represented only one spanwise slice of the airfoil. Symmetric boundary conditions were applied to the sides of the mesh, i.e. one single VGJ is explicitly resolved, while the interaction was modeled via the symmetry. The circular VGJ orifice was also explicitly resolved; a special “actuation boundary condition” was applied inside the orifice, which allowed treating the jet as compressible.

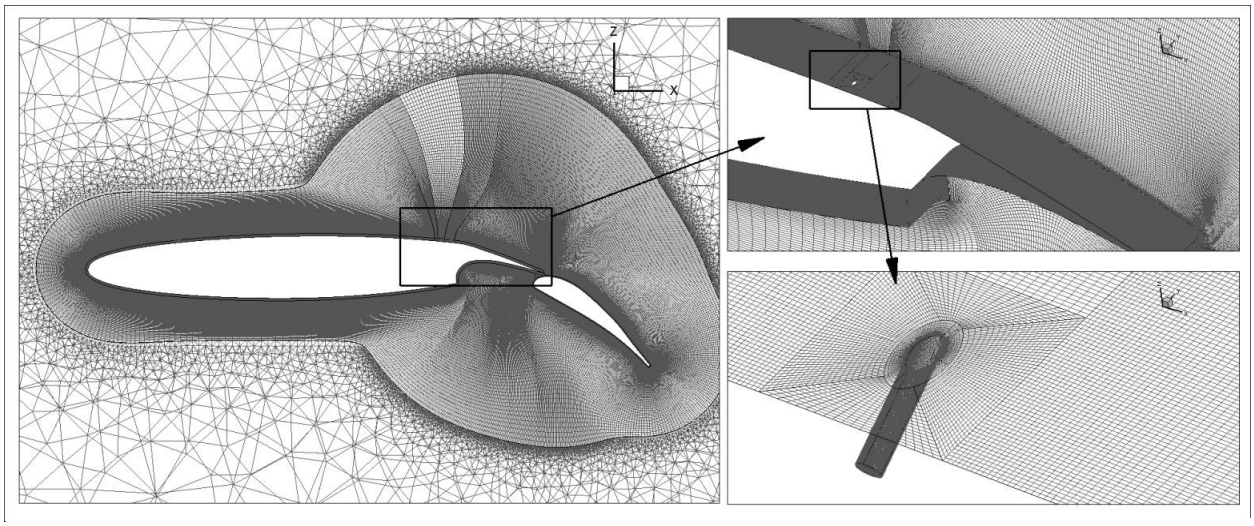

Figure 1: Hybrid structured/unstructured grid for the RANS-studies with resolved VGJs and vortices

Grid density was based on refinement studies, the turbulent stresses were modeled with the MSST k-ω-model. Both, grid density and turbulence model were validated against experimental data. A dual time-stepping scheme resolving defined steps in (physical) time was applied for numerical stability.

The outcomes of the RANS computations with resolved vortices were time-averaged flowfields. This detailed flow information was utilized for calibration of the statistical approach as will be explained below in Figure 3. It might be noted that it was beyond the scope of the studies to comprehensively vary the VGJ configuration, which instead was based on previous experience, [7][8][9][10]. Nevertheless, also some sensitivity studies were performed with the fully resolved approach, the reader is referred to deliverable D2.3 for more details.

3.2 Design Studies with the Statistical Model (WP 2, T2.2, T2.4)

The key enabler for meaningful design studies of high-lift configurations including the effect of flow control is the ability to include the latter into computations without the need for extensive computational power. Here, the effect of the VGJs, i.e. the effect of the longitudinal vortices on the mean flow, were modeled by the approach of von Stillfried et al. [13][14]. Neither the jet, nor the generated vortices are resolved in this type of computation. Instead, the influence of the vortices on the mean flow was captured through the spanwisely averaged vortex stresses $\langle u_i u_j \rangle$. These act similar as the Reynolds stresses for turbulence and were captured by an additional source term in the turbulence model. In the present case, where the flow is statistically periodic in the spanwise direction, the VGJ model computations can be performed in 2D RANS computations within an optimization loop—actually not even a severely refined mesh is required in the respective area.

3.2.1 Model Calibration

For a modeling of the VGJs the generated vortices are parameterized w.r.t. the jet parameters. In a preprocessor the vortices are represented by the velocity field of a Lamb-Oseen vortex, where Γ (circulation), r_0 (viscous core radius) as well as the wall-to-core distance h_c are then correlated by three coefficients to the VGJ operational and/or geometrical parameters. The velocity field of the vortex, u_i, u_j, is then averaged in spanwise direction, where also the symmetry (representing the spanwise array) is accounted. The averaging gives the vortex stresses $\langle u_i u_j \rangle$. Once added at the position of the VGJs, the normal turbulence model transports the vortex stresses as in every RANS-solution process.

For model calibration, the three coefficients were varied to match the averaged velocity field downstream of the VGJs that comes from the fully resolved computations. Figure 2 shows the model computations for three downstream positions compared with the averaged fully resolved computations for an angle of attack of 4°. The “kink” in the velocity profile near the vortex core cannot be fully captured by the present modeling approach. Moreover, the downstream development of the vortex is more diffused by the model. An interesting fact should be noted, that is that the model was well able to capture the influence of different jet exit velocities with the same set of model coefficients.

Figure 3 shows the effect of the VGJs on the lift curve, based on a yet arbitrary flap/spoiler configuration. The left subfigure shows the baseline case and two lift curves including the effect of the VGJs at two different jet exit velocities 245 m/s and 305 m/s. The right sub-figure shows basically the same configurations, but the data was acquired with the fully resolved approach.

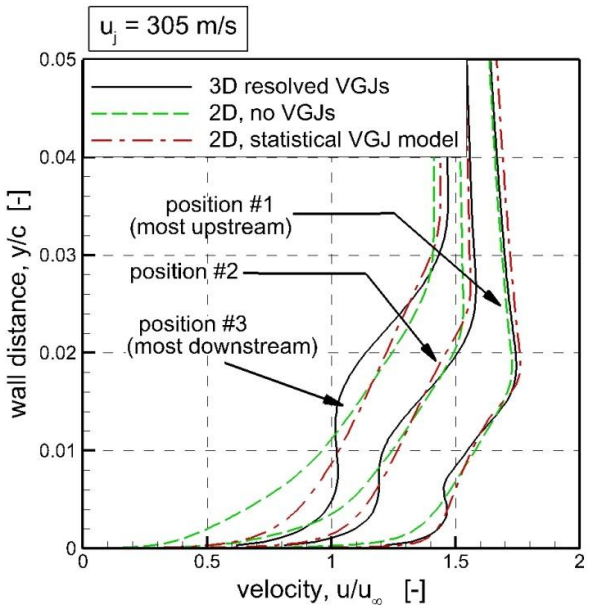

Figure 2: Boundary layer velocity profiles at three positions downstream of the VGJs

Such computations with the statistical model are well able to capture the general phenomenology of VGJ-application. The maximum lift is increased by about 0.2, which is in line with the fully resolved computations. Also the relative effect of the amplitude of blowing is captured well. Although notable differences remain, e.g. the effect of the VGJs on the AoA of maximum lift is weaker for the statistically

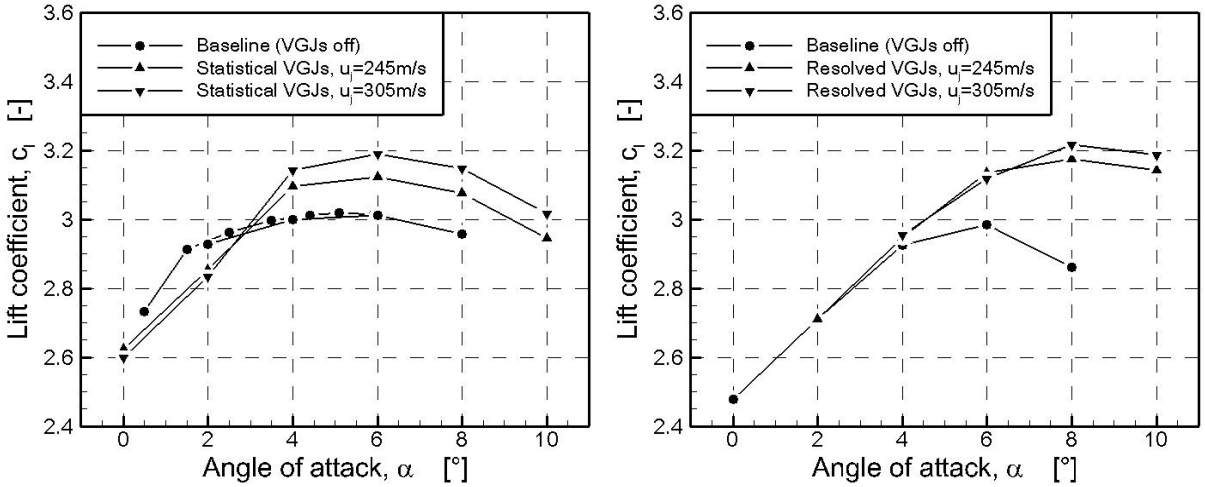

Figure 3: Lift coefficient vs. angle of attack for different VG jet velocities; Numerical data based on statistical VGJ approach (left) and based on resolved VGJs (right)

modeled VGJs, is should be noted here, that the difference in computational effort between each computation in the right subfigure and the left subfigure is two days on a multi-processor supercomputer cluster vs. two hours on a standard home PC. Thus, the statistical model is a key enabler for optimization studies including the effect of the VGJs.

3.2.2 Design Studies

The design of configurations to account for active flow control was done by a differential evolution algorithm, [17]. The cost function was rather straightforward, high lift values at a fixed AoA of 5° were

favored, whereas oscillations of lift (either unphysical due to numerical instability or physical due to near stall) and a non-linear lift curve between 0° and 5° were penalized. The free parameters have been varied through different optimization runs, typically the geometrical parameters spoiler droop angle, flap angle, gap and overlap were considered.

Opt 1	Flap setting (angle, gap and overlap) and spoiler droop angle only. No flow control.
Opt 3	Flap setting (angle, gap and overlap), spoiler droop angle and FG jet angle. Fix FG jet velocity and thickness. No VG jet.
Opt 4	Same as Opt3 but with reduced FG jet velocity.
Opt 6	Flap setting (angle, gap and overlap) and spoiler droop angle. No FG jet. Fix VG jet position and parameters.
Opt 7	Flap setting (angle, gap and overlap) and spoiler droop angle. Fix FG jet from Opt3. Fix VG jet position and parameters.

Table 1: Optimization Studies

The starting point for assessing the potential benefits of flow control was to optimize the baseline flap setting without flow control but including the spoiler droop angle. The resulting geometry is referred to as Opt1—it gave a flap deflection of 42.2° together with a spoiler droop angle of 12.8°. The corresponding lift curve, refer to Figure 4, shows a smooth distribution with an almost constant increased lift for all angles of attack compared with the initial D10 setting. Such typical optimization of 5 to 6 parameters uses a population of 25. A reasonable good convergence towards an optimal solution was reached after around 40 iterations. This means around 1000 function evaluations with 2 CFD computations in each (two AoA, since non-linearity of the lift curve was penalized).

The same cost function and optimization procedure was used to optimize the flap setting and spoiler droop with the FG at the main element trailing edge and the VGJs just upstream of the spoiler kink. Opt 3 and 4 covered FG only, Opt 6 is VGJ only and Opt 7 is both combined. A separate optimization was done to find the best position for the VGJ (not shown here). The VGJ parameters were the same as in the resolved RANS computations, because currently the model is not fully calibrated/validated to reflect different VGJ settings. Throughout all simulations the model coefficients were set to represent a standard setting for the VGJs at a jet exit velocity of 305 m/s, or a jet momentum coefficient of $C\mu \approx 0.2$, respectively.

Figure 4 summarizes the outcome of the optimization studies. Opt 1 (configurational setting only, no AFC) has already some increased maximum lift as compared to D10, since D10 was chosen more-or-less arbitrary and it was expected that there is some potential. Opt 3 and Opt 4 are cases with the FG only (with different amplitude), where it can be seen that the FG has a good potential to increase maximum lift. Opt 6 is the case with the VGJs operative only (no FG). Compared to Opt 3 and Opt 4 the Opt 6 uses only roughly one third of the effort in terms of C_μ, so the VGJs are apparently more efficient, though the effect is a little less in $C_{L,max}$ compared to the FG. Finally, if both is used together, it turns out that the effect of the two AFC-methods is roughly summable. The effectiveness of the system is very remarkable, with both actuations a $C_{L,max}$ of almost 3.7 can be reached, which is a benefit of more than 0.5 compared to the reference case of the airfoil with only a spoiler droop.

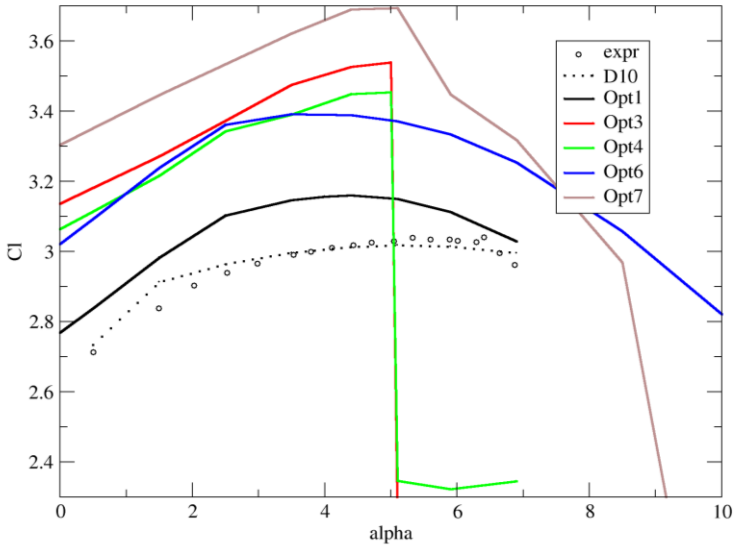

Figure 4: Lift curves resulting from the optimization cases

4 Validation Experiment (WP3)

4.1 Experimental Setup

For the measurements a new main element of the wind tunnel model with DLR-F15 contour was constructed and manufactured. The wind tunnel model has a reference chord length of *c*=600mm with retracted flap. The wing span is *b*=1.3m. The wind tunnel model consists of the new main wing, utilizing an existing flap. The shroud is equipped with vortex generator jets (VGJs) at x/c=0.69 and fluidic gurneys (FGs) 0.8mm upstream of the trailing edge of the main element. The droop of the shroud or rather the spoiler can be changed by several inserts (marked red Figure 5) to vary the angle of the droop. This allows to use the same FGs in the three tested drooped spoiler configurations. The configuration fs#1 is the non-drooped configuration, opt7 and rot11 are two different drooped configurations.

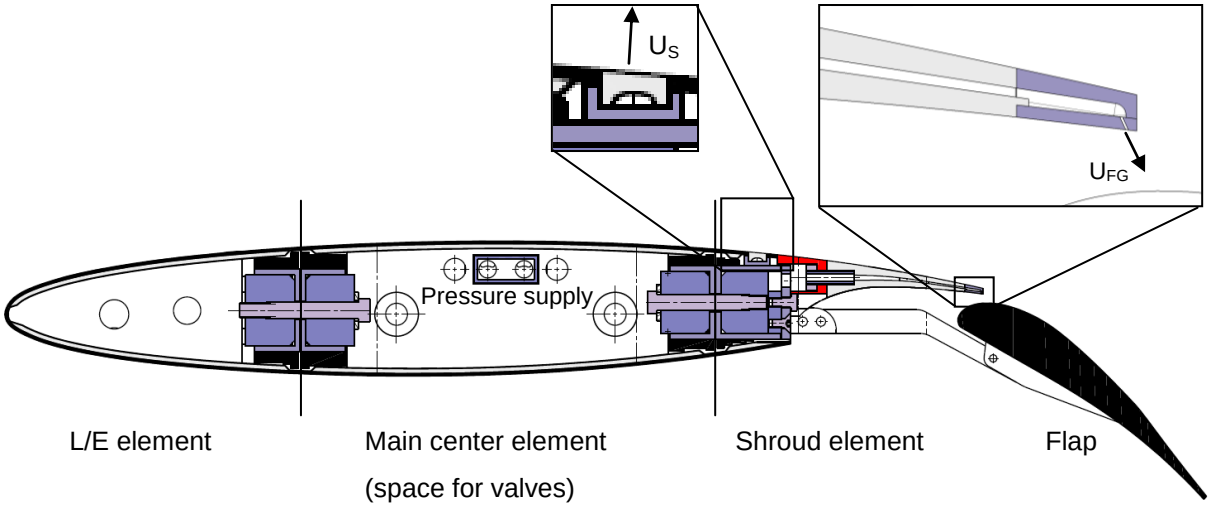

Figure 5: Cut view of the main wing.

Setting	Spoiler angle	Flap angle	Flap gap	Flap overlap
fs#1	0.000°	40.064°	5.089mm	13.885mm
opt7	20.700°	48.500°	16.080mm	20.640mm
rot11	10.705°	50.769°	5.089mm	16.384mm

Table 2: Tested configurations.

The measurements were conducted in the wind tunnel "Modell Unterschallwindkanal Braunschweig" (MUB) of the institute of fluid mechanics of the Technische Universität Braunschweig. It is a closed circuit wind tunnel with a 5.7m long test section. The cross section has a size of 1.3m x 1.3m. The free stream velocity during the measurements was U_∞=50m/s which results in a Reynolds number of Re=1.8·10^6 and a Mach number of M=0.14. For the experimental results, normal force coefficients cnp will be presented, because in the experimental entry the drag was not measured, thus—by definition--the normal force cannot be converted into lift. It might however be noted that normal force coefficient c_{np} and lift coefficient c_L are very similar (typically differ by less than 4%).

4.2 Results

The measured normal force curve of the non-drooped configuration fs#1 with transition fixing is presented in Figure 6a. The reference fs#1 is a reference for all configurations because it is numerically optimized for high lift coefficients without active flow control (AFC). The configuration opt7 without AFC is also presented in Figure 6a and is named as reference opt7. The normal force curve is shifted to a lower value. With active FGs no positive influence is observed. With increasing momentum coefficient the maximum normal force coefficient is reduced. Also, this is not generally unexpected. Since the FGs act on the flow downstream of the flap gap. If the drooped spoiler is separated, the flow cannot be "healed" by the FGs.

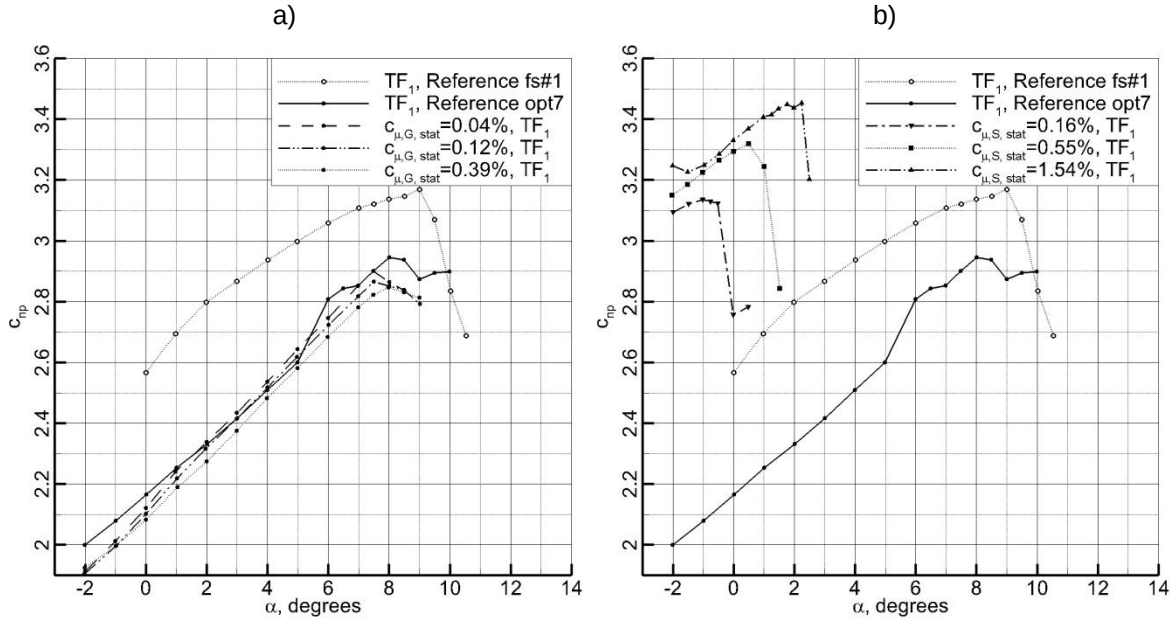

Figure 6: Normal force curves measured with a) active FGs and b) active VGJs. Non-filled symbols: non-drooped configuration; Filled symbols: drooped configuration

Figure 6b visualizes the influence of the VGJs. The momentum coefficient varies between $c_{\mu,S,stat}$=0% and $c_{\mu,S,stat}$=1.54%. With increasing momentum coefficient the normal force coefficient as well as the maximum normal force coefficient increases. The AoA of the maximum normal force coefficient is lower than the references fs#1 and opt7. A comparison of the normal force curves without and with maximum momentum coefficient shows that in the linear part of the normal force curve benefits of up to Δc_{np}=1.25 and $\Delta c_{np,max}$=0.51 are measured. A comparison with the reference fs#1 indicates benefits of up to Δc_{np}=0.76 and $\Delta c_{np,max}$ =0.28. The corresponding AoA of the maximum normal force coefficient also increases with increasing momentum coefficient but it is lower than the references fs#1 and opt7.

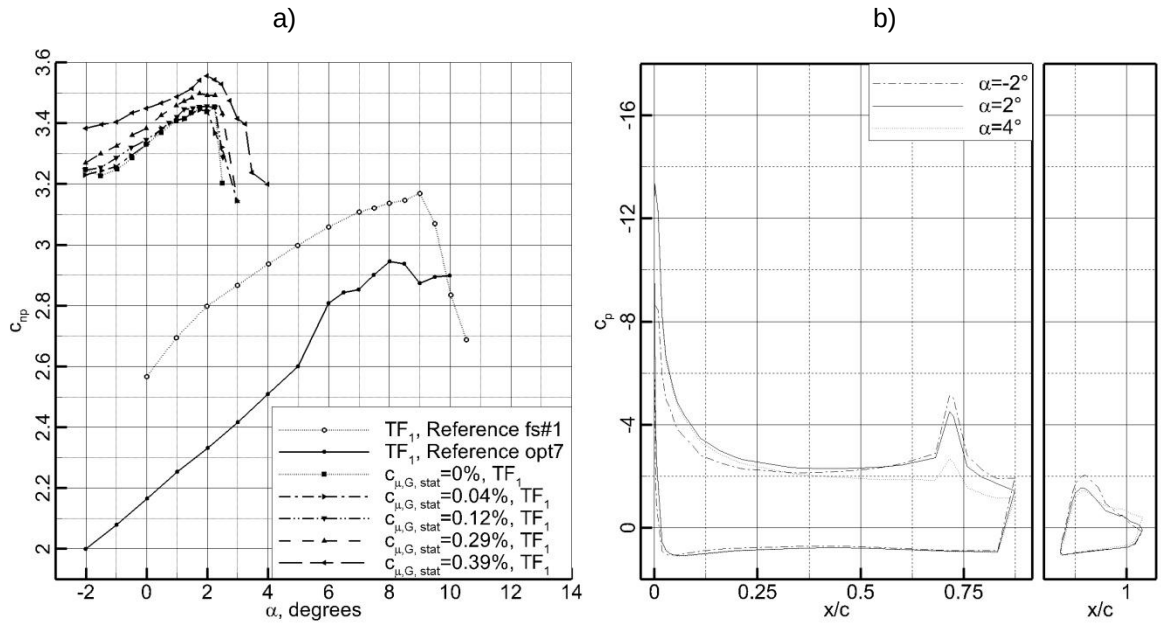

Figure 7: Normal force coefficient (a) with active VGJs ($c_{\mu,S}$=1.54%) and FGs ($c_{\mu,G}$=[0.04, 0.12, 0.29, 0.39]%) and pressure distribution (b) with active VGJs ($c_{\mu,S}$=1.54%) and FGs ($c_{\mu,G}$=0.39%). Non-filled symbols: non-drooped configuration; Filled symbols: drooped configuration

Combined blowing of the VGJs and FGs results in the normal force curves as presented in Figure 7a. The VGJs are blowing with a momentum coefficient of $c_{\mu,S,stat}$=1.54%. The momentum coefficient of the FGs varies between $c_{\mu,G,stat}$=0% and $c_{\mu,G,stat}$=0.39%. Higher momentum coefficients are not possible. An influence of the FGs with momentum coefficients of up to $c_{\mu,G}$=0.12% is not visible. The results are similar to the normal force curve with inactive FGs. This behaviour changes with increasing momentum coefficient and an increase of the normal force coefficient was measured. Compared with inactive FGs a momentum coefficient of $c_{\mu,G}$=0.39% increases the normal force coefficient and the maximum normal force coefficient by a value of approximately $\Delta c_{np,max} \approx 0.1$.

The pressure distribution of the best AFC test case with $c_{\mu,S,stat}$=1.54% and $c_{\mu,G}$=0.39% at three AoA is presented in Figure 7b. At α=-2° the strong suction peak at the front part of the spoiler indicates an attached flow on the spoiler. The flap also has a strong suction peak. At α=2° the suction peak at the nose increases whereas the suction peaks at the spoiler and the flap decrease. At α=4° the suction peak at the nose of the main wing is still high. The small suction peak at spoiler and the decreased pressure at the trailing edge of the flap indicate flow separations on the rear part of the main wing and the rear part of the flap. Thus, the normal force coefficient is limited by a trailing edge stall at an AoA of α=2°.

The influence of the VGJs in the configuration rot11 is shown in Figure 8a. The momentum coefficient varies between $c_{\mu,S,stat}$=0.16% and $c_{\mu,S,stat}$=1.54%. An increase of the momentum coefficient results in an increased normal force coefficient as well as maximum normal force coefficient. Also the AoA of the maximum normal force coefficient increases but is lower than the references fs#1 and opt7. Comparing the normal force curves of the measurements without and with blowing shows that in the linear part of the normal force curves benefits of up to Δc_{np}=1.02 and $\Delta c_{np,max}$=0.67 are achieved. A comparison with the reference fs#1 indicates benefits of Δc_{np}=0.64 and $\Delta c_{np,max}$=0.30. It should be noticed that the maximum normal force coefficients with active VGJs are similar to the results of the configuration opt7 with active VGJs but the maximum AoA with attached flow are higher. However, the configuration opt7 has the potential for higher normal force coefficients at higher AoA due to the higher camber. The numerical optimizations for this configuration opt7 predicts an AoA of α=5° with higher c_μ. The simulations are done with c_μ=1.3% and the maximum of the actual design is c_μ=0.39% which is only one third.

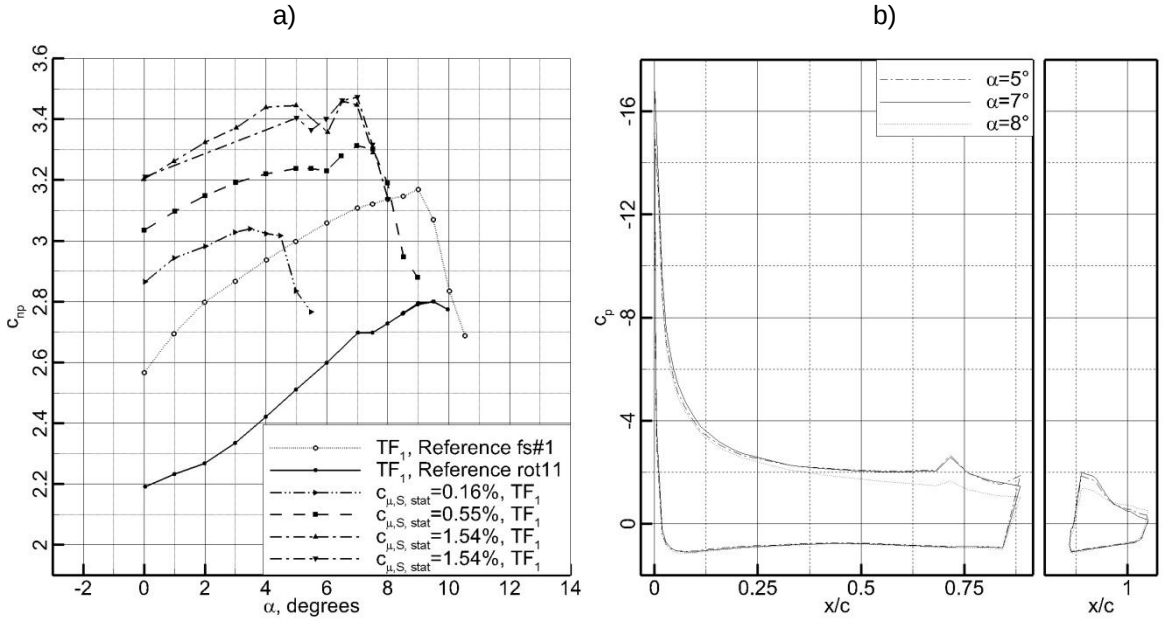

Figure 8: Normal force coefficients measured with active VGJs ($c_{\mu,S}$=[0.16, 0.55, 1.54]% (a) and (b) pressure distributions measured with highest momentum coefficient ($c_{\mu,S}$=1.54%). Non-filled symbols: non-drooped configuration; Filled symbols: drooped configuration

Figure 8b visualizes pressure distributions of the configuration rot11 with maximum blowing VGJs ($c_{\mu,S}$=1.54%). From α=5° to α=7° the suction peaks on main wing and flap increases and the flow at the drooped spoiler is attached. The stalled airfoil at α=8° still has a reduced suction peak at the nose of the main wing. The pressure at the suction peak of the flap and the rear part of the main wing increases. This indicates a trailing edge stall.

Both drooped configurations (opt7 and rot11) are limited by a trailing edge stall and it seems that the VGJs are the flow control device to increase the AoA of the maximum normal force coefficient.

5 Comparison between Experimental and Numerical Results

In the experiments the C_μ needed to be chosen very different from the numerical design studies, because determination is a matter of post-processing and post-calibration of the AFC-system. Also, configurational changes are hard to realize in the experiment, therefore variations (e.g. variation of AFC method between VGJs and FG, amplitude variations) have been done with the Opt 7 setting and an additional setting called ROT 11. In order to put the experimental data into context, in WP 2, T2.6, the exact experimental cases were re-calculated using the numerical method with the statistical model described above.

Figure 9 summarizes some core results of the experimental entry, along with the nominally same cases recalculated using the numerical approach with statistical VGJs as described above. The left subfigure shows results at a flap setting Opt 7, which features 20.8° of spoiler droop and a 48.5° flap. The right subfigure shows results for the setting Rot 11, which is a rather moderate setting with only 10.7° of spoiler droop, but a highly deflected high lift flap with a flap angle of 50.8°.

For both (baseline, i.e. no active VGJs) settings the flap and the spoiler region was largely separated in the experiment. The numerical results show significant deviation from the experimental data, which is often found for cases with large separated areas. In the case of the ROT 11 baseline setting the numerical computations actually predict an attached spoiler flow at lower AoA, which then gradually detaches, while in the experiments the spoiler was separated.

In both cases, Opt7 as well as ROT 11, the VGJs up-stream of the drooped spoiler are able to (re-) attach the flow over the spoiler surface, thus significantly increasing the lift. In all three cases (Opt7 with lower and higher C_μ and Rot11 with higher C_μ) the numerical computations first predict a partly

separated flap at lower AoA, which then reattaches for the AoA of maximum lift. In these cases, again, there are some arguable differences between the results of the numerical computations and the experimental data. However, it can also be concluded that the statistical VGJ-model is able to predict the $C_{l,max}$, since this value matches quite well for all three cases with active VGJs. The reason, why many values do not match, but finally $C_{l,max}$ agrees, is that most of the cases have dominant separations at AoA different than the one of maximum lift.

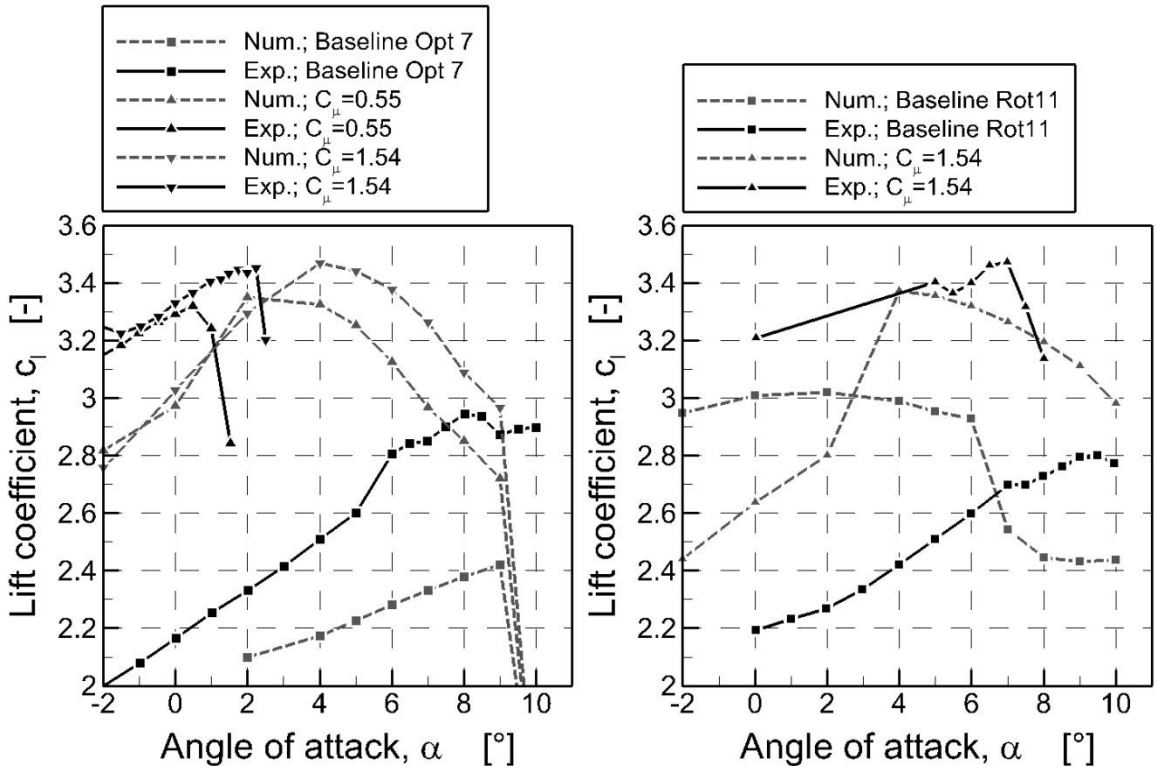

Figure 9: Comparison between measured lift curves and simulations using the statistical VGJ-model; Left: Configuration "Opt7" with different VGJ-C_μ; Right: Configuration "Rot11"

6 Spoiler Kink Smart Surface (WP 1)

6.1 Concept Development

While the application of the VGJs upstream of the spoiler kink allows an extensively lowered element, still a sharp kink should be avoided. This requires a smart surface that smoothes the kink, when the spoiler is drooped. However, the spoiler has to fulfil its original designation to act as an air break by deploying upwards.

Here, a system called the "cogging design" is proposed: The trailing region of the upper surface panel of the main wing element and the leading edge of the spoiler panel feature cogs. The distance between these two elements is linked by an additional cog-element. The center cog-element is mounted such that an upward motion (spoiler air break mode) is not obstructed, since the different pieces allow rotation into one direction. In the case of downward motion (droop spoiler mode) the leading and trailing panels restrict the center element, which will consequently bend and thus generate a smooth transition between the main upper panel and the spoiler surface.

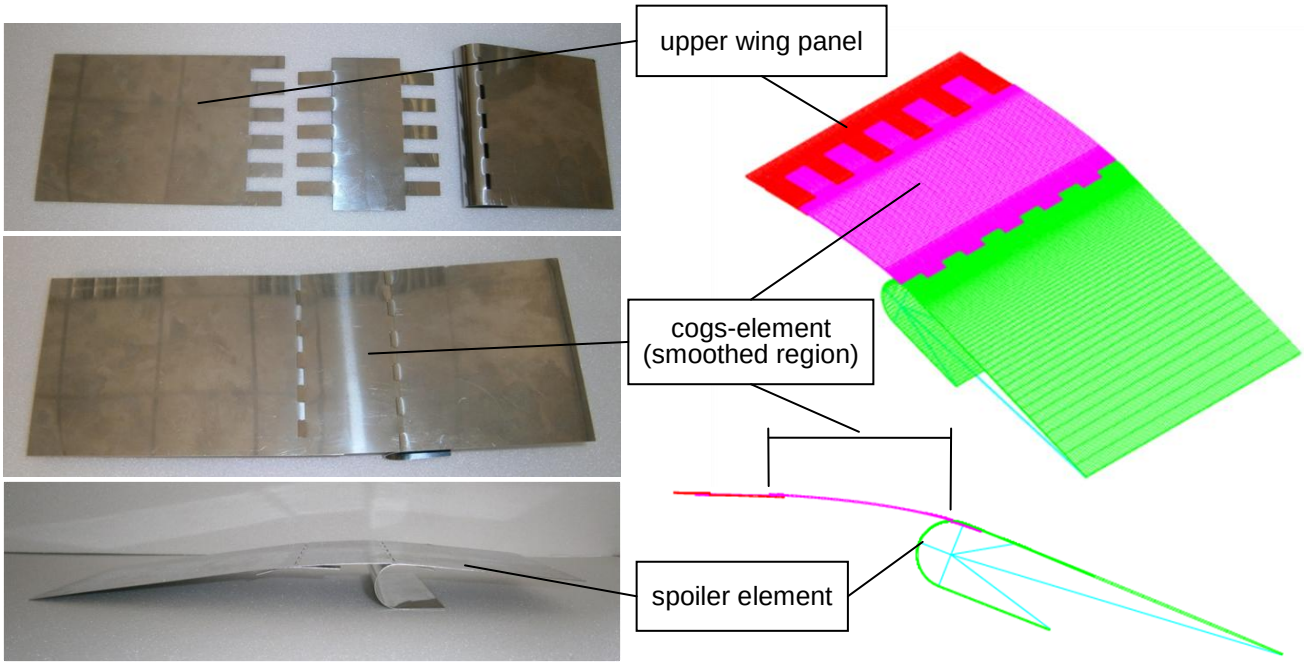

Figure 10: Small-scale test piece demonstrating the principle of the cogging-design
Left: Proof-of-concept test-piece Right: FEM-model indicating the curvature of the bended cogging element

It might be noted that the above aerodynamic testing was performed with an upper surface representing a realistic cogging area. The smooth transition area was validated in detail using a large-scale demonstrator including the cogging mode, which will be discussed in the next subsection. At first Figure 10 highlights the concept. The airbrake-setting of the spoiler can be generated without additional forces or loads. In the neutral setting the cogs-element connects the spoiler and the upper wing panel with a straight line. Due to the individual cogs the surface features two serrated lines with alternating forward- and backward-facing steps. These steps have the dimension of the panel thickness and are indeed a certain disturbance to the flow, but will be small for a full-size aircraft. In the current case the cogs-sizes have been synchronized to the VGJs, such that the vortices trailing downstream interact with these small steps symmetrically.

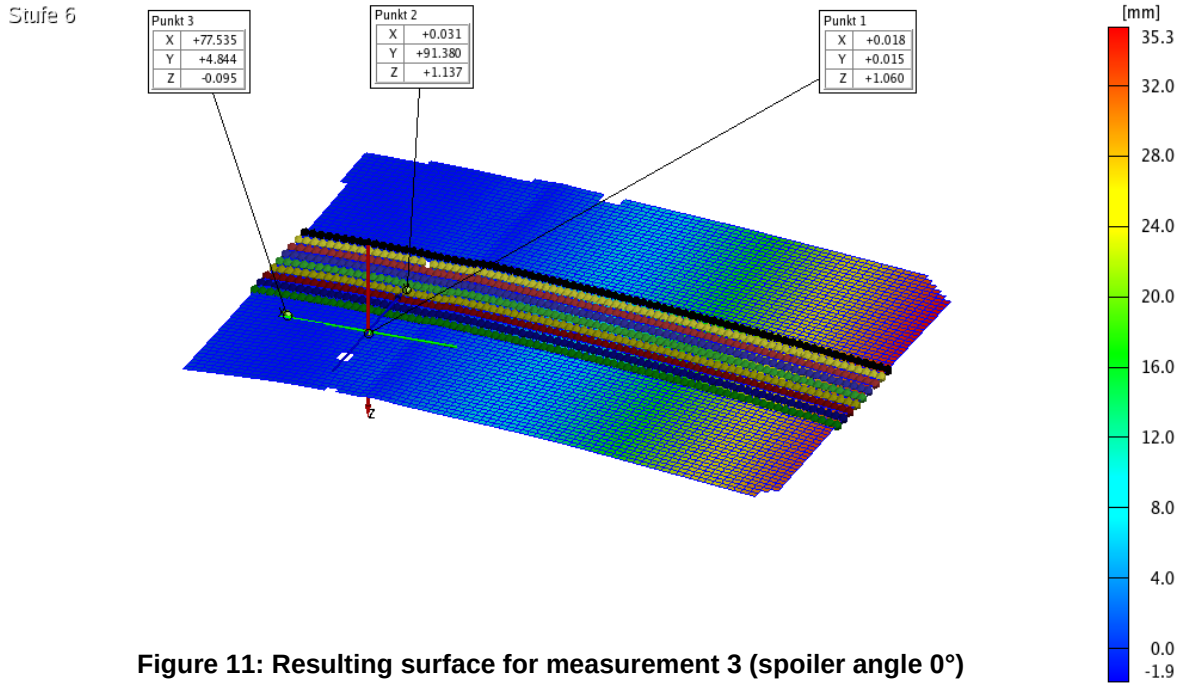

Figure 11: Resulting surface for measurement 3 (spoiler angle 0°)

6.2 Demonstrator Results

During the demonstration measurements the spoiler droop was manually set to different values, starting from upward motion (negative angles) going to downward motion/ spoiler droop (positive angles, see Table 1). A number of spoiler-angles was chosen in the field of measurement. Special attention was given to the spoiler droop/ positive angles since here the smart surface has to be effective. Some angles for the upward motion were also measured in order to have an idea how the structure would cope with these angles. The results will be shown in this section as an example for one angle in detail.

The surface of the cogging-model was inspected by an optical surface scanning system of type ARAMIS, which utilizes a stereo-camera-setup to track a random-pattern applied on the surface. After the ARAMIS-pictures were taken and analyzed using the post-processing steps of the ARAMIS-software. As a result, the three-dimensional surface is available for further analysis. The result for a spoiler-angle=0° can be seen in Figure 11.

Figure 12 shows a plot of the resulting curve that is created by extracting the cut-line visible in Figure 11. A magnification of the transition area is also provided in order to highlight were the cogged-sheet is actually working. Two small discontinuities are seen. The left continuity is of about 1mm height and is linked to the step introduced by the cog itself. The right step is slightly higher and depicts the other end of the cog-sheet, namely the interface with the spoiler. In this point the thickness step due to the transition of the cogged sheet into the spoiler through the gap in the spoiler-leading edge is visible.

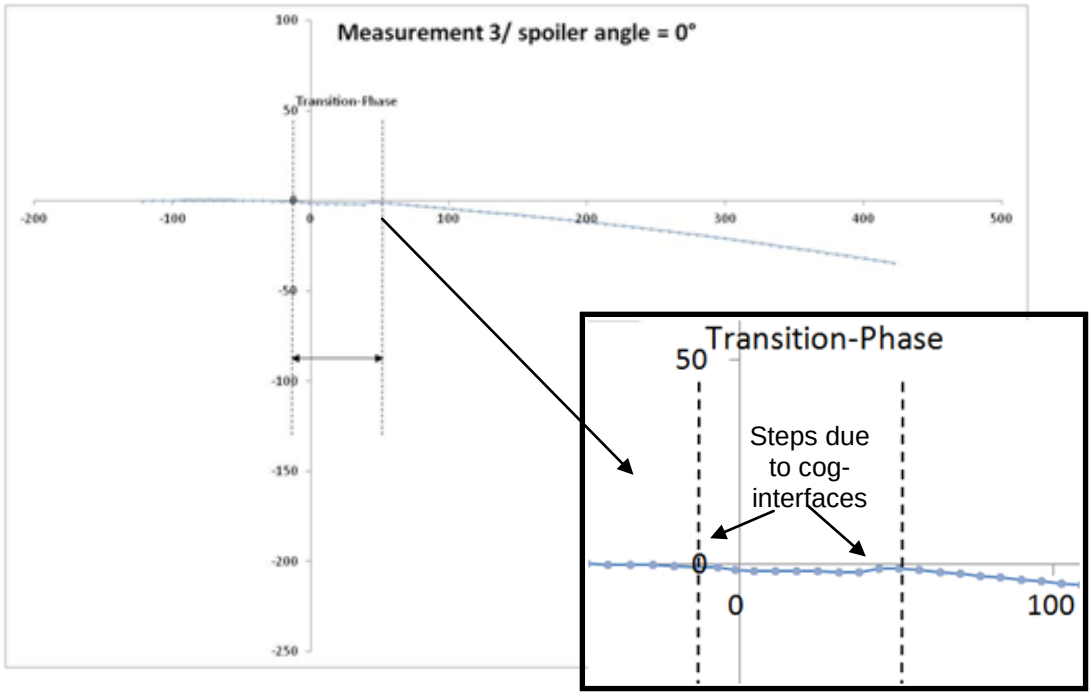

Figure 12: Plot of a cut through the measured contour for angle 0° (all dimensions in mm)

Figure 14 shows the behaviour of the structure for a spoiler angle of 21°. This angle was the highest droop angle to be tested. Again, a similar behaviour is visible. In the area in which the cogged sheet is placed a small step due to the cogs is visible. Apart from that the overall behaviour is very smooth, even for higher spoiler droop angles the system is working fine.

Figure 13 shows a detailed view on the sheet/ spoiler interface. It can be seen that at the location of the gap the spoiler-surface is slightly bending up, causing a discontinuity. This is due to a simplification of the demonstrator design in that region: The spoiler leading-edge is realized by bending a sheet metal plate, which is

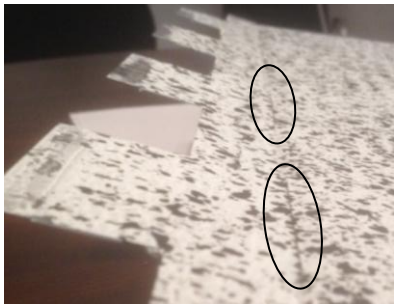

Figure 13: Detailed view on sheet/spoiler interface

difficult to control with thin material. The gaps for the cogs have been laser-cut before the bending. Therefore it is very difficult to ensure that the cogs smoothly fit into the spoiler-element at the upper part of the leading-edge, where even small misalignments result in a discontinuity. Nevertheless, the impact on the whole concept is not a very big one and for an industrial application approaches to overcome this situation have been presented in the exploitation report, D4.2.

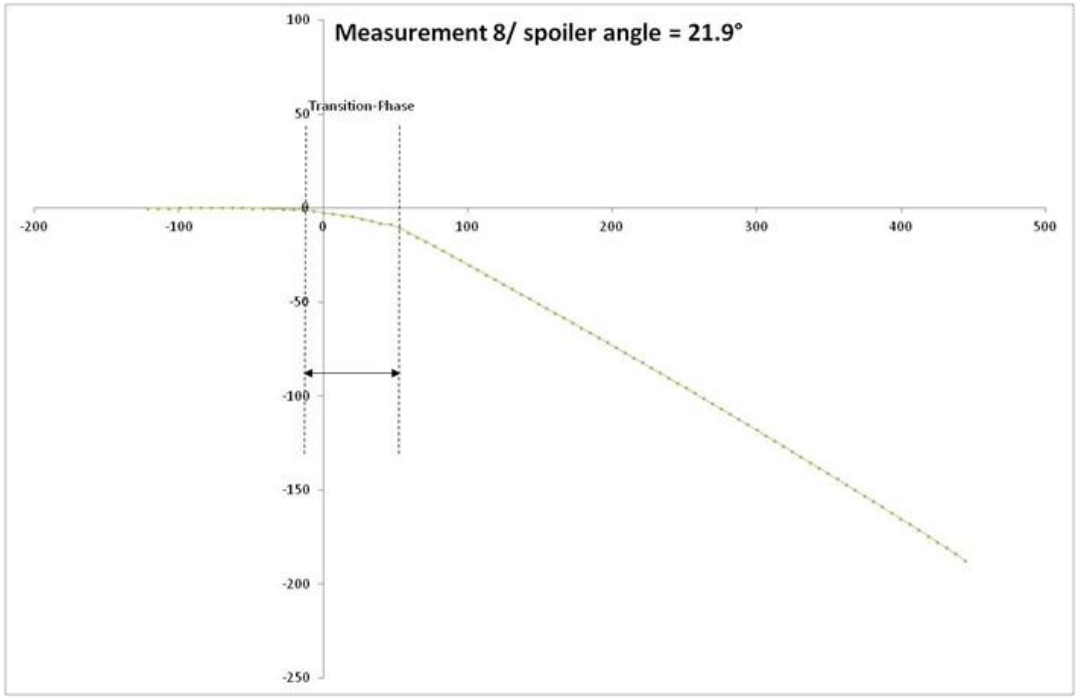

Figure 14: Contour at a spoiler angle of 21.9° (all dimensions in mm)

7 References

[1] Scholz, P., Mahmood, S.S., Casper, M., Wallin, S., Skoogh, D., Adden, S., Design of Active Flow Control at a Drooped Spoiler Configuration, AIAA-2013-2518, 31st AIAA Applied Aerodynamics Conference, 24-27 Jun 2013, San Diego, USA

[2] Johnston, J.P., Nishi, M., Vortex Generator Jets--Means for Flow Separation Control, AIAA Journal, Vol. 28, No. 6, pp. 989--994, 1990

[3] Mahmood, S., Radespiel, R., RANS simulation of jet actuation in a boundary layer flow using Chimera grids, Deutscher Luft- und Raumfahrtkongress, Aachen, Germany, 8--10 Sep 2009

[4] McManus, K., Legner, H.H., Davis, S.,J., Pulsed Vortex Generator Jets for Active Control of Flow Separation, AIAA Paper 94-2218, 25th AIAA Fluid Dynamics Conference, Colorado Springs, USA, 20--23 June 1994

[5] Ortmanns, J., Bitter, M., Kähler, C.J., Dynamic vortex structures for flow-control applications, Experiments in Fluids, Vol. 44, No. 3, pp. 397-408, 2008

[6] Wild, J., Experimental investigation of Mach- and Reynolds-number dependencies of the stall behavior of 2-element and 3-element high-lift wing sections, Journal of Aircraft, Vol. 50, No. 4, pp. 1202-1216, 2013

[7] Scholz, P., Casper, M., Ortmanns, J., Kähler, C.J., Radespiel, R., Leading Edge Separation Control by Means of Pulsed Vortex Generator Jets, AIAA Journal, Vol. 46, No. 4, 2008, pp. 837--846

[8] Casper, M., Scholz, P., Radespiel, R., Separation Control on an Airfoil with Vortex Genera-tor Jets, KATnet II Conference on Key Aero-dynamics Technologies, 12--14 May 2009, Bremen, Germany

[9] Mahmood, S., Scholz, P., Radespiel, R., Numerical Design of Leading Edge Flow Control over Swept High-Lift Airfoil, 3rd CEAS Air & Space Conference & 21st AIDAA Congress, 24--28 October 2011,

[10] Scholz, P., Kähler, C.J., Radespiel, R., Wild, J., Wichmann, G., Active Control of Leading-Edge Separation within the German Flow Control Network, AIAA 2009-529, 47th AIAA Aero-space Sciences Meeting Including The New Horizons Forum and Aerospace Exposition, 5--8 January 2009, Orlando, Florida, USA

[11] Wild, J., Wichmann, G., Haucke, F., Peltzer, I., Scholz, P., Large scale separation flow control experiments within the German Flow Control Network, AIAA 2009-530, 47th AIAA Aerospace Sciences Meeting Including The New Horizons Forum and Aerospace Exposition, 5--8 January 2009, Orlando, Florida, USA

[12] Schwamborn, D., Gerhold, T., Heinrich, R., The DLR TAU-Code: Recent Applications in Research and Industry, in: P. Wesseling, E. Oate, J. Priaux (Eds), ECCOMAS CFD, Egmond aan Zee, The Neherlands, 2006

[13] von Stillfried, F., Johansson, A.V., Wallin, S., A Statistical Vortex-Generator-Jet Model for Turbulent Flow-Separation Control, AIAA Journal Vol. 51, No. 5, pp. 1119–-1129, 2013

[14] von Stillfried, F., Johansson, A.V., Wallin, S., Vortex-Generator Models for Zero- and Ad-verse-Pressure-Gradient Flows, AIAA Journal Vol. 50, No. 4, pp. 855-–866, 2012

[15] von Stillfried, F., Wallin, S., Johansson, A.V., Ortmanns, J., Casper, M., Evaluating and Pa-rameterizing Round Vortex Generator Jet Experiments for Flow Control, AIAA Journal, Vol. 50, No. 11, pp. 2508-–2524, 2012

[16] Eliasson, P., Edge, a Navier-Stokes solver for unstructured grids, Proceedings of Finite Volumes for Complex Applications III, edited by D. Kroner and R. Herbin, Hemre Penton Science London, 2003

[17] Storn, R., Price, K., Differential evolution: a simple and efficient heuristic for global optimization over continuous spaces, Journal of global optimization, Vol. 11, pp. 341--359, 1997